Figure S1. (A) The fiberoptic NNOM sensor probed the head with two sets of source-detector separations; $\rho_l = 3.2$ cm and $\rho_s = 0.7$ cm for sequential TR-NIRS measurements of the cerebral absorption coefficient at 6 wavelengths (*i.e.,* $\mu_{a,c}(\lambda)$, for $\lambda = 730, 770, 786, 810, 830, 850$ nm), and $\rho_{l,f} = 2.5$ cm and $\rho_s = 0.7$ cm for the DCS measurement of the cerebral blood flow index (F_c). These non-invasive measures were compared to invasive *PbtO$_2$*, *TDF CBF*, *ICP*, and microdialysis regional measurements made through the quad-lumen bolt. A two-layer tissue model of the head was used for NNOM analysis, which is composed of a semi-infinite bottom layer (*i.e.,* cortical regions of brain) and a superficial top layer (*i.e.,* scalp/skull tissue) with thickness *L*. The top layer blood flow index, absorption coefficient, and reduced scattering coefficient are F_{ec}, $\mu_{a,ec}$, and $\mu_{s,ec}'$, respectively. The bottom layer properties are F_c, $\mu_{a,c}$, and $\mu_{s,c}'$. **(B)** Exemplar TR-NIRS measurements of the temporal point spread functions ($\Phi(T)$, see text) for the long (red solid curve) and short (blue dashed curve) source-detector separations ($\lambda = 810$ nm, 800 ms exposure), as well as the instrument response function (IRF, black solid line, see text) obtained on a post ischemic-anoxic encephalopathy patient. **(C)** Exemplar DCS measurements (same patient) of the normalized intensity autocorrelation functions ($g_2(\tau)$) for the long (red circles) and short (blue x-marks) source-detector separations (averaged across 10-seconds, also 15 channels for $\rho_{l,f}$).

NNOM Analysis Approach

Details about the hybrid time resolved near-infrared spectroscopy (TR-NIRS) and diffuse correlation spectroscopy (DCS) optical instrumentation used for this study are provided elsewhere.[1] The TR-NIRS technique delivers short near-infrared light pulses (<100 ps) to a source position on the scalp. At two detectors separated at distances $\rho_l = 3.2$ cm and $\rho_s = 0.7$ cm from the source, the so-called temporal point spread functions (*i.e.,*

$\Phi_t(T,\rho_l)$, $\Phi_t(T,\rho_s)$) were measured. The temporal point spread function is a histogram of the number of photons striking the detector as a function of the "time of flight", T, between the source trigger and photon detection, at measurement time t (see Figure S1(B)). The TR-NIRS instrument response function (IRF) was also measured as described elsewhere.[1]

The DCS technique measures temporal speckle intensity fluctuations of coherent near-infrared light that has scattered from moving red blood cells in the volume of tissue traversed by the light (*i.e.,* from source to detector).[2, 3] These temporal fluctuations are quantified by computing the normalized intensity temporal autocorrelation function, $g_2(\tau,\rho) \equiv \langle I(t,\rho)I(t+\tau,\rho)\rangle / \langle I(t,\rho)\rangle^2$, at multiple delay-times, τ (see Figure S1(C)). Here, $I(t,\rho)$ is the detected light intensity at time t and source-detector separation ρ, and the angular brackets, $\langle\rangle$, represent time-averages (*i.e.,* 10 seconds in this study). DCS measurements were obtained at two source-detector separations, $\rho_{l,f} = 2.5$ cm and $\rho_s = 0.7$ cm (see supplemental Figure S1(C). For the $\rho_{l,f}$ separation, 15 independent measurements obtained in parallel with 15 detection channels were averaged together to improve signal-to-noise ratio. As described in the main manuscript, we employed a two-layer model of the head to derive a cerebral blood flow index (F_c) from the $g_2(\tau,\rho_{l,f})$ and $g_2(\tau,\rho_s)$ measurements.[4]

It is desirable to fit the TR-NIRS temporal point spread functions ($\Phi_t(T,\rho)$) at every measurement time to the two-layer analytical solution of the photon diffusion equation in order to extract the absorption and reduced scattering coefficients for the cerebral and extra-cerebral tissue layers. However, we could not reliably implement this approach in practice. Since the width of the short separation temporal point spread function was comparable to the width of the instrument response function, accurate nonlinear fitting with

the short separation was difficult. Nonlinear fitting of 4 parameters from only one source-detector separation measurement is further prone to cross talk between the parameters. Accordingly, we used a paradigm that derived cerebral absorption coefficient changes from changes in moments of $\Phi_t(T,\rho)$.

For each $\Phi_t(T,\rho)$ in a time series, the background signal, defined as the mean number of photons measured prior to the initial rise of the $\Phi_t(T,\rho)$, was subtracted. The kth moment for time t and source-detector separation ρ is defined as $m_{k,t}(\rho) \equiv \int_{T_1}^{T_2} T^k \Phi_t(T,\rho)\mathrm{d}T$, where the integration limits T_1 and T_2 are established by $\Phi_o(T_1,\rho)=0.01\Phi_o(T_{max},\rho)$ $(T_1<T_{max})$ and $\Phi_o(T_2,\rho)=0.03\Phi_o(T_{max},\rho)$ $(T_2>T_{max})$, respectively. Here, $\Phi_o(T_{max},\rho)$ is the maximum photon count (at time of flight bin T_{max}) for the baseline temporal point spread function, $\Phi_o(T,\rho)$ (i.e., average of $\Phi_t(T,\rho)$ across the baseline time interval). Note, photons with long time of flights are more sensitive to the cortical layer, but the use of a very large upper integration limit, T_2, in practice leads to large errors from background noise.[5, 6] The choice of the integration limits for moments used here was based on previous work that investigated optimal limits for cortical measurement.[5]

Previous work has further demonstrated that the variance of the temporal point spread function, i.e., $V_t(\rho) = m_{2,t}(\rho)/m_{0,t}(\rho)-(m_{1,t}(\rho)/m_{0,t}(\rho))^2$, is more sensitive to cortical tissue than the lower order moments.[7-9] A time-domain variant of the two-layer Modified Beer-Lambert formulation was used to derive changes in $V(\rho_l)$ measurements at the long TR-NIRS separation (ρ_l) induced by changes in extra-cerebral and cerebral tissue absorption:[7, 10, 11]

$$\Delta V(\rho_l) = vsf_{ec}(\rho_l)\Delta\mu_{a,ec} + vsf_c(\rho_l)\Delta\mu_{a,c}. \qquad \text{(A1)}$$

Here, $\Delta V(\rho_l) = V_t(\rho_l) - V_o(\rho_l)$, $\Delta\mu_{a,c} = \mu_{a,c}(t) - \mu_{a,co}$, and $\Delta\mu_{a,ec} \equiv \mu_{a,ec}(t) - \mu_{a,eco}$ are the differential changes in the variance moment, cerebral tissue absorption, and extra-cerebral tissue absorption, respectively, between time t and baseline. The multiplicative weighting factors $vsf_{ec}(\rho_l) \equiv \partial V_o(\rho_l)/\partial\mu_{a,ec}$ and $vsf_c(\rho_l) \equiv \partial V_o(\rho_l)/\partial\mu_{a,c}$ were computed numerically via

$$vsf_{ec} \approx \frac{\tilde{V}\left(\rho_l, \mu_{a,co}, \mu_{a,eco} + \Delta\mu_{a,ec}/2, \mu'_{s,co}, \mu'_{s,eco}\right) - \tilde{V}\left(\rho_l, \mu_{a,co}, \mu_{a,eco} - \Delta\mu_{a,ec}2, \mu'_{s,co}, \mu'_{s,eco}\right)}{\Delta\mu_{a,ec}},$$

$$vsf_c \approx \frac{\tilde{V}\left(\rho_l, \mu_{a,co} + \Delta\mu_{a,c}/2, \mu_{a,eco}, \mu'_{s,co}, \mu'_{s,eco}\right) - \tilde{V}\left(\rho_l, \mu_{a,co} - \Delta\mu_{a,c}2, \mu_{a,eco}, \mu'_{s,co}, \mu'_{s,eco}\right)}{\Delta\mu_{a,c}}, \quad (A2)$$

where $\Delta\mu_{a,ec}/\mu_{a,eco} = \Delta\mu_{a,c}/\mu_{a,co} = 0.1$, and $\tilde{V}$ is the variance moment computed with the two-layer time-domain Green's function solution of the photon diffusion equation, G.[12]

Specifically, $\tilde{V} = \tilde{m}_2/\tilde{m}_0 - (\tilde{m}_1/\tilde{m}_0)^2$, where $\tilde{m}_k = \int_{T_1}^{T_2} T^k G(T, \rho, \mu_{a,c}, \mu_{a,ec}, \mu'_{s,c}, \mu'_{s,ec}, L)dT$

(integration limits T_1 and T_2 defined above with $G(T, \rho, \mu_{a,co}, \mu_{a,eco}, \mu'_{s,co}, \mu'_{s,eco}, L)$ in lieu of $\Phi_o(T,\rho)$). Note, Equation (A1) assumes constant tissue scattering, and is most accurate for small tissue absorption changes.

In the present analysis, L was obtained from patient anatomical CT scans at the rough position where the NNOM sensor was placed. In addition, for the computation of $vsf_{ec}(\rho_l)$ and $vsf_c(\rho_l)$, we assumed that $\mu_{a,eco} = \mu_{a,co} = \mu_{a,semi}$ and $\mu'_{s,eco} = \mu'_{s,co} = \mu'_{s,semi}$, where $\mu_{a,semi}$ and $\mu'_{s,semi}$ are the tissue absorption and scattering coefficients obtained from nonlinear fit of $\Phi_o(T,\rho)$ to the convolution of the IRF with the semi-infinite Green's function solution of the photon diffusion equation.[13] Note, we followed a nonlinear fitting procedure described elsewhere,[14] wherein the launch time of the incident source pulse on

tissue, t_0, was constrained in the fit to be within ±50 ps of the time point when the measured IRF maximum occurs. A homogeneous tissue index of refraction of 1.4 was also assumed.

Finally, we applied the Modified Beer-Lambert law to the short separation data, i.e., $\Phi_t(T, \rho_s)$, to compute the extra-cerebral tissue absorption change in Equation (A1):[15-17]

$$\Delta\mu_{a,ec} = \Delta OD(\rho_s) / mpp_{ec}(\rho_s). \qquad (A3)$$

Here, $\Delta OD(\rho_s) = OD_t(\rho_s) - OD_o(\rho_s)$, $OD_t(\rho_s) \equiv -\log(m_{0,t}(\rho_s))$, $m_{0,t}(\rho_s)$ is the zero order moment for the short separation, and the differential pathlength, $mpp_{ec}(\rho_s) \equiv \partial OD_o(\rho_s)/\partial\mu_{a,ec}$, was computed analytically with the semi-infinite solution of the continuous-wave photon diffusion equation (for optical properties $\mu_{a,semi}$ and $\mu'_{s,semi}$ defined above).[18] Equation (A3) assumes that $\Delta OD(\rho_s)$ is only sensitive to the extra-cerebral tissue layer. Note, since the width of the IRF was comparable to the width of the short-separation temporal point spread function on tissue, reliable absolute optical properties could not be obtained from the short separation data.

In summary, for each TR-NIRS wavelength, $vsf_c(\rho_l)$, $vsf_{ec}(\rho_l)$, and $\Delta\mu_{a,ec}$ obtained from Equations (A2) and (A3) were substituted into Equation (A1) to solve for $\Delta\mu_{a,c}$. As described in the main manuscript, the concurrent $\Delta\mu_{a,c}$ at the 6 TR-NIRS wavelengths are used to estimate relative changes in oxygen extraction fraction (Equation (2)). The constant tissue scattering assumption in this analysis is often reasonable during hemodynamic concentration variations,[19] but it also can lead to errors if tissue structure substantially changes (e.g., edema). For the case examples reported in this work, temporal variations in $\mu'_{s,semi}$ were <5%. The approximation of equal tissue optical properties for the extra-cerebral and cerebral tissue layers at baseline can also result in errors in the computation of the vsf_c, vsf_{ec}, and mpp_{ec} sensitivity factors in Equations (A2) and (A3). As

a first exploration of the magnitude of these errors, we computed different sensitivity factors using a cerebral absorption coefficient that was 10% higher than $\mu_{a,semi}$ for the ischemia case example (Figure 2A). We then used these sensitivity factors to compute the fractional oxygen extraction fraction change (i.e., rOEF).

We found that a 10% underestimation in the cerebral absorption coefficient resulted in a 5% underestimation in the maximal rOEF reached. Similarly, a 25% underestimation in absorption resulted in a 10% underestimation in rOEF, and a 50% underestimation in absorption resulted in a 30% underestimation in rOEF. Thus, this exploratory analysis suggests that errors in the baseline tissue optical properties translate to smaller fractional errors in rOEF changes. Future work is needed to investigate these errors more completely. In many clinical situations, the absolute magnitude of the change may be less important than the indication of substantial hemodynamic changes (**Table S1**).

**Table S1.** Potential Clinical Applications of NNOM

Disease Entity	Physiologic Issue	Use of NNOM
Subarachnoid Hemorrhage	Vasospasm	Detect ischemia
Intracranial Hypertension	Can be caused by hyperemia or edema	Differentiate hyperemic vs oligemic intracranial hypertension
Ischemic stroke	Post thrombectomy infarct expansion or hemorrhage	Detect ischemic or hyperemic contributors
Intracerebral hemorrhage	Hemorrhagic expansion	Detect decreased CBF with increased OEF
Post cardiac arrest	Dysautoregulation	Determine optimal MAP to optimize autoregulation
Carotid stenosis	Monitoring during CEA	Detect ischemia and hyperemia during and post cross clamp
Cardiac surgery	Monitoring during CPB	Detect ischemia and hyperemia to guide pump management and make transfusion decisions based on OEF
Traumatic Brain Injury	Brain edema	Optimize MAP and PaCO2 based on CBF and OEF data

*This table provides examples and is an incomplete listing of potential applications.
CEA-carotid endarterectomy; CPB-cardiopulmonary bypass; MAP-mean arterial pressure; CBF-cerebral blood flow; OEF-oxygen extraction fraction

Comparison of Two-Layer and Semi-infinite Tissue Models

Figure S2 is a comparison of the relative blood flow (rBF≡BF/BF$_o$) and oxygen extraction fraction (rOEF≡OEF/OEF$_o$) changes computed with the two-layer head model (i.e., used for the paper) and with semi-infinite techniques for the ischemic (panel **A**), hypermetabolic (panel **B**), and hyperemic (panel **C**) case examples reported in the main manuscript. BF$_o$ and OEF$_o$ are the baseline (mean) values between the two vertical red lines. The 2-layer results (i.e., red circles) are the results presented in the main manuscript (i.e., **Figures 2, 3**). The "semi-infinite" results (i.e., blue squares) for rBF were obtained from fitting the DCS signals acquired at the long separation (i.e., $g_2(\tau,\rho_{l,f})$; **Figure S1**) to the homogeneous semi-infinite tissue model.[4] The semi-infinite results for rOEF were obtained by using a homogeneous version of Equation (A1):
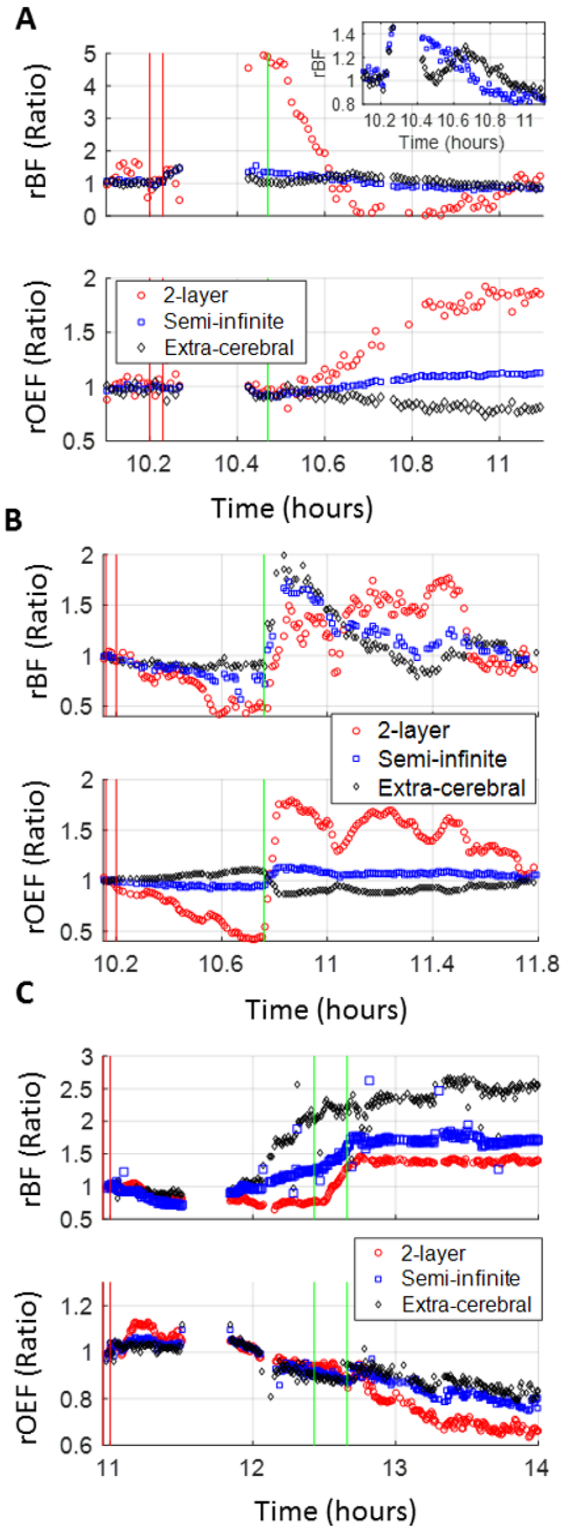
Figure S2.

$$\Delta V(\rho_l) = vsf_{semi}(\rho_l)\Delta\mu_{a,semi}. \tag{A4}$$

Here, $vsf_{semi} \approx \left(\tilde{V}_s\left(\rho_l, \mu_{a,semi} + \Delta\mu_{a,semi}/2, \mu'_{s,semi}\right) - \tilde{V}_s\left(\rho_l, \mu_{a,semi} - \Delta\mu_{a,semi}/2, \mu'_{s,semi}\right)\right) \Big/ \Delta\mu_{a,semi}$,

where the baseline semi-infinite tissue optical properties $\mu_{a,semi}$ and $\mu'_{s,semi}$ are defined in the previous section, and $\tilde{V}_s$ is the variance moment computed with the semi-infinite time-domain Green's function solution of the photon diffusion equation (analogous to the two-layer moment discussed below Equation (A2)). The concurrent $\Delta\mu_{a,semi}$ at the 6 TR-NIRS wavelengths were converted to rOEF (i.e., Equations (1), (2)). Finally, the extra-cerebral results (i.e., black diamonds) were computed from application of the same semi-infinite analysis techniques to the short separation DCS and TR-NIRS signals.

For all 3 case examples in **Figure S2**, the direction of the blood flow and oxygen extraction fraction trends obtained from the long-separation semi-infinite analysis are consistent with the two-layer results. The magnitudes of the changes, however, are substantially smaller, especially for the ischemic case example in panel A. Further note that the direction of the extra-cerebral blood flow and oxygen extraction fraction trends are not always consistent with the two-layer results. For the hyperemia case example in panel C, the direction of the short separation changes was consistent, but for panels A and B, the extra-cerebral OEF change is in the opposite direction of the two-layer OEF change. Thus, the short separation measurements alone cannot detect the ischemic, hypermetabolic, and hyperemic conditions reported herein. The long separation semi-infinite results can potentially distinguish between these directions, but as expected, this analysis shows the semi-infinite results experience substantial contamination from extra-cerebral tissue.

References

1.	He L, Baker WB, Milej D, et al. Noninvasive continuous optical monitoring of absolute cerebral blood flow in critically ill adults. *Neurophotonics*. 2018; 5: 045006.
2.	Boas DA, Campbell LE and Yodh AG. Scattering and Imaging with Diffusing Temporal Field Correlations. *Physical Review Letters*. 1995; 75: 1855-8.
3.	Boas DA and Yodh AG. Spatially varying dynamical properties of turbid media probed with diffusing temporal light correlation. *J Opt Soc Am A*. 1997; 14: 192-215.
4.	Baker WB, Parthasarathy AB, Ko TS, et al. Pressure modulation algorithm to separate cerebral hemodynamic signals from extracerebral artifacts. *Neurophotonics*. 2015; 2: 035004-.
5.	Liebert A, Wabnitz H, Grosenick D, Moller M, Macdonald R and Rinneberg H. Evaluation of optical properties of highly scattering media by moments of distributions of times of flight of photons. *Appl Opt*. 2003; 42: 5785-92.
6.	Steinkellner O, Gruber C, Wabnitz H, et al. Optical bedside monitoring of cerebral perfusion: technological and methodological advances applied in a study on acute ischemic stroke. *Journal of biomedical optics*. 2010; 15: 061708.
7.	Liebert A, Wabnitz H, Steinbrink J, et al. Time-Resolved Multidistance Near-Infrared Spectroscopy of the Adult Head: Intracerebral and Extracerebral Absorption Changes from Moments of Distribution of Times of Flight of Photons. *Appl Opt*. 2004; 43: 3037-47.
8.	Liebert A, Wabnitz H, Steinbrink J, et al. Bed-side assessment of cerebral perfusion in stroke patients based on optical monitoring of a dye bolus by time-resolved diffuse reflectance. *Neuroimage*. 2005; 24: 426-35.
9.	Milej D, Janusek D, Gerega A, et al. Optimization of the method for assessment of brain perfusion in humans using contrast-enhanced reflectometry: multidistance time-resolved measurements. *J Biomed Opt*. 2015; 20: 106013.
10.	Liebert A, Wabnitz H and Elster C. Determination of absorption changes from moments of distributions of times of flight of photons: optimization of measurement conditions for a two-layered tissue model. *J Biomed Opt*. 2012; 17: 057005.
11.	Steinbrink J, Wabnitz H, Obrig H, Villringer A and Rinneberg H. Determining changes in NIR absorption using a layered model of the human head. *Physics in Medicine and Biology*. 2001; 46: 879.
12.	Liemert A and Kienle A. Application of the Laplace transform in time-domain optical spectroscopy and imaging. *J Biomed Opt*. 2015; 20: 110502.
13.	Kienle A and Patterson MS. Improved solutions of the steady-state and the time-resolved diffusion equations for reflectance from a semi-infinite turbid medium. *Journal of the Optical Society of America A, Optics, image science, and vision*. 1997; 14: 246-54.
14.	Selb J, Joseph DK and Boas DA. Time-gated optical system for depth-resolved functional brain imaging. *J Biomed Opt*. 2006; 11: 044008.
15.	Delpy DT, Cope M, Zee Pvd, Arridge S, Wray S and Wyatt J. Estimation of optical pathlength through tissue from direct time of flight measurement. *Physics in Medicine and Biology*. 1988; 33: 1433.
16.	Arridge SR, Cope M and Delpy DT. The theoretical basis for the determination of optical pathlengths in tissue: temporal and frequency analysis. *Physics in Medicine and Biology*. 1992; 37: 1531.

17.   Hiraoka M, Firbank M, Essenpreis M, et al. A Monte Carlo investigation of optical pathlength in inhomogeneous tissue and its application to near-infrared spectroscopy. *Phys Med Biol*. 1993; 38: 1859-76.

18.   Fantini S, Hueber D, Franceschini MA, et al. Non-invasive optical monitoring of the newborn piglet brain using continuous-wave and frequency-domain spectroscopy. *Physics in Medicine and Biology*. 1999; 44: 1543.

19.   Baker WB, Parthasarathy AB, Busch DR, Mesquita RC, Greenberg JH and Yodh A. Modified Beer-Lambert law for blood flow. *Biomed Opt Express*. 2014; 5: 4053-75.